Materials Advances

ROYAL SOCIETY OF CHEMISTRY

PAPER

View Article Online
View Journal | View Issue

Cite this: *Mater. Adv.*, 2025, **6**, 7609

Nickel oxide-modified nickel foam current collectors for uniform lithium deposition at the anode

Hao He,[ab] Zhao Yu,[c] Yongsheng Hu,[a] Shenmin Zhu,[a] Yanyu Li,[a] Yanjie Liu,[a] Yue Miao,[a] Yao Li*[a] and Di Zhang[a]

Received 24th June 2025,
Accepted 8th September 2025

DOI: 10.1039/d5ma00669d

rsc.li/materials-advances

Lithium metal anodes, possessing a high theoretical specific capacity of 3860 mAh g^{-1} and a low potential (−3.04 V *vs.* the standard hydrogen electrode), represent a promising direction for advanced energy-storage technology. Nevertheless, the uncontrolled dendritic growth of lithium metal, resulting in poor reversibility and substantial volume changes, significantly impedes the practical implementation of lithium metal batteries. This study introduces nickel oxide nanoparticles as lithiophilic sites on the 3D skeleton of nickel foam (NF) as a 3D current collector (NF-NiO) to promote dendrite-free Li deposition. The NiO nanoparticles effectively modulated Li–metal deposition morphology, reducing the formation of multiple interfacial layers that could cause phase separation and high electrochemical polarization. The nickel foam annealed at 450 °C (NF-NiO450) as a current collector achieved an average Li–metal plating/stripping Coulombic efficiency (CE) of 97.7% for 330 cycles, significantly outperforming neat NF (~96.6%), which lasted only 75 cycles. The $LiFePO_4$‖NF-NiO450 (prelithiated to a negative-to-positive areal capacity ratio, N/P ratio ≈ 1.51) cell demonstrated superior rate capability and maintained 92.42% capacity retention over 160 cycles. This engineered 3D current collector design advances the development of high-energy, long-life lithium metal batteries.

1. Introduction

The metallic Li anode has attracted considerable attention due to its high theoretical specific capacity (3860 mAh g^{-1}), low density (0.59 g cm^{-3}) and low potential (−3.04 V *vs.* the standard hydrogen electrode).[1–6] It is recognized as one of the most promising anode materials for high-voltage and high-energy batteries.[3,5,6] However, a major challenge lies in the disordered growth of lithium dendrites.[1,7,8] During lithium deposition, non-uniform electric field distribution across the electrode surface creates irregular lithium-ion flow patterns, forming dendrites, which may penetrate the separator and trigger battery short circuits.[7,9] When the adhesion between lithium dendrites and the current collector is insufficient, these dendrites may detach during cyclic mechanical stress, becoming "dead Li" as they become encapsulated by the electron-insulating solid–electrolyte interface (SEI).[10–13] This phenomenon compromises both cell safety and performance longevity.

Three-dimensional (3D) skeletons exhibiting high electronic conductivity and mechanical flexibility have emerged as promising substrates for efficient lithium stripping/plating. These 3D structures, featuring extensive active surface area for Li deposition, effectively reduce applied current density and accommodate mechanical cyclic stress during Li stripping and plating. Submicron-sized skeletons, porous structures, and 3D copper/lithium composite electrodes have demonstrated effectiveness as 3D current collectors.[2,3,14,15] However, their complex manufacturing processes and potential high costs may limit their practical implementation. Thus, developing 3D current collectors using commercially viable materials and straightforward preparation methods remains essential.

Commercial metal foams, featuring 3D interconnected structures and robust mechanical properties, present a viable foundation. Beyond their 3D architecture, material selection criteria should favor metals resistant to forming irreversible or electrochemically unstable alloys with Li, thereby preventing active Li loss through detrimental dealloying reactions. Analysis of various metal–Li phase diagrams led to the selection of nickel, which exhibits non-alloying behavior with Li and benefits from existing commercial foam production. However, Ni displays limited lithiophilicity due to its non-alloying nature with Li. To promote uniform Li plating within the Ni foam, NiO

[a] *State Key Laboratory of Metal Matrix Composites, School of Materials Science and Engineering, Shanghai Jiao Tong University, Shanghai, 200240, China. E-mail: liyaosjtu@sjtu.edu.cn*
[b] *Zhiyuan College, Shanghai Jiao Tong University, Shanghai, 200240, China*
[c] *Department of Chemical and Materials Engineering, University of Alberta, 9211-116 Street NW, Edmonton Alberta T6G 1H9, Canada*

nanoparticles were incorporated onto the Ni surface, utilizing the strong polarity of metal–oxygen bonds and conversion reaction with Li.

$$NiO + 2Li \rightarrow Li_2O + Ni$$

This reaction is highly favorable and occurs *in situ*, replacing the original NiO with a composite material composed of nano-sized metallic Ni particles embedded within a Li_2O matrix, which is inherently lithiophilic and serves as a good Li-ion conductor, facilitating smooth Li-ion flux across the surface.[19,20] As a metal with a body-centered cubic structure,[21,22] Li electrodeposition proceeds through initial nucleation followed by peripheral growth.[23–25] Li adatoms preferentially aggregate in low surface energy regions, forming atomic nuclei that develop into needle-shaped lithium dendrites.[25–28] The nickel oxide surface modification generates Li_2O during solid–electrolyte interphase (SEI) formation, providing high interfacial energy that inhibits lithium dendrite growth.[29–32] Enhanced surface energy promotes lithium atom self-diffusion on the substrate and facilitates higher-dimensional nucleation.[22]

This study presents a method for preparing nickel oxide-modified nickel foam current collectors (NF-NiO) through direct growth of nickel oxide particles on the substrate *via* acid washing and air-annealing processes. The multiple oxidation states of nickel demonstrate excellent coordinating ability, preventing the formation of multiple interfaces during lithium deposition and regulating the deposition morphology.[3] Different annealing temperatures were selected to control the ratio of NiO and Ni_2O_3 phases. The results indicate that the designed nickel foam current collector (NF-NiO) effectively achieves homogeneous Li plating without apparent dendrite formation (Fig. 1). Compared to unmodified NF and nickel oxide-modified nickel foam electrodes annealed at other temperatures, the nickel oxide-modified nickel foam annealed at 450 °C (NF-NiO450) exhibited enhanced half-cell cycling life, achieving 220 cycles with Coulombic efficiency (CE) of 97.3% at 2 mA cm^{-2} and 1 mAh cm^{-2}. A full-cell utilizing NF-NiO450 as the anode and $LiFeO_4$ as the cathode maintained a capacity retention rate of 92.42% for over 160 cycles at a 1C rate with a (N/P) ratio of 1.51, demonstrating superior cycle reversibility.

2. Experimental section

2.1. Material synthesis – preparation of the nickel oxide-modified nickel foam current collector (NF-NiO)

Nickel foam of 0.5 mm thickness was punched into 12 mm diameter discs using a punching machine, followed by ultrasonication in ethanol solution for 10 minutes and subsequent drying. The NF discs underwent immersion in 1 mol L^{-1} HCl solution for 1 hour to eliminate surface impurities. After rinsing with deionized water to remove HCl, the discs were immersed in 2 mol L^{-1} HNO_3 solution and agitated for 4 h.[33–35] The NF was then extracted, rinsed thoroughly with deionized water three times to remove residual acid and impurities. The discs were subsequently dried in a vacuum drying oven at 90 °C for 12 h to ensure complete moisture removal. The dried NF discs were placed in a ceramic crucible and heated in a muffle furnace at 400 °C, 450 °C, and 500 °C for 4 h each in an air atmosphere, with a heating rate of 2 °C min^{-1}. After cooling to room temperature, the resulting nickel oxide-modified nickel foam substrates were designated as NF-NiO.

2.2. Characterizations for NF-NiO

Scanning electron microscopy (SEM) images were obtained using a JSM-7800F operated at 5 kV, equipped with an energy dispersive spectrometer (EDS) operating at 15 kV for component analysis. The crystalline structures were analyzed using an X-ray diffractometer (XRD, Rigaku D/max2550VL) with a filtered Cu Kα radiation source. X-ray photoelectron spectroscopy (XPS) was conducted on an AXIS UltraDLD (Shimadzu). Due to the sensitivity of lithium-deposited anodes to moisture and oxygen, sample preparation and analysis were performed in an argon glove box. Samples extracted from coin cells were washed three times with dimethyl ether (DME) and dried under vacuum for two hours before XPS or SEM analysis.

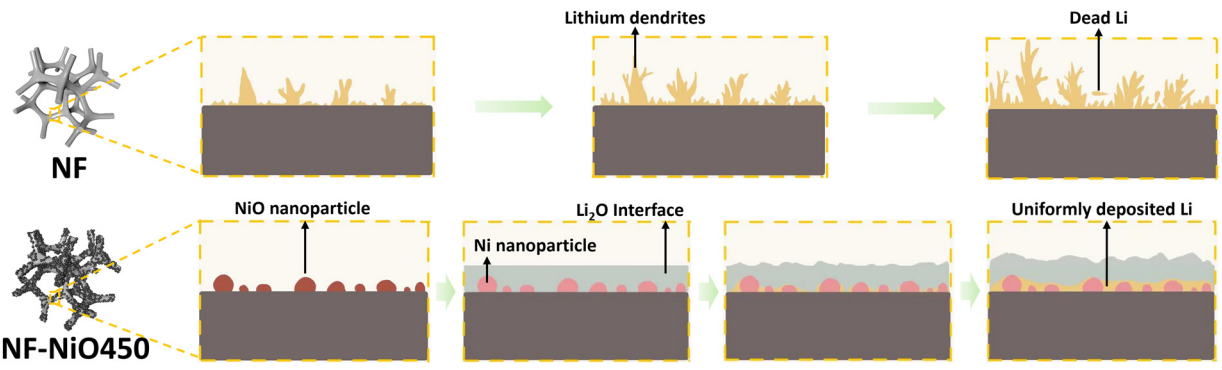

Fig. 1 Schematic illustrating the lithium metal deposition behavior on 3D materials NF and NF-NiO. Li nucleation within NF pores effectively reduces volumetric expansion compared to planar current collectors. The smooth NF framework surface, however, generates localized electric field heterogeneity, leading to isolated dendritic lithium formations. Conversely, the NF-NiO architecture exhibits enhanced lithiophilicity through strongly polar Ni–O bonds that act as active nucleation sites. Li_2O produced by the reaction has strong lithiophilicity, promoting the uniform deposition of Li.[4,12,16–18]

2.3. Electrochemical measurements

The CR-2032 cell was employed for CE and full-cell property testing, assembled in an argon-filled glove box (MBRAUN, $O_2 <$ 0.1 ppm, $H_2O <$ 0.1 ppm). Cu foil, NF and NF-NiO served as current collectors and were assembled with Li metal as the reference/counter electrode. The electrolyte consisted of 70 μL of 1 M lithium bis(trifluoromethanesulfonyl)imide (LiTFSI) dissolved in 1,3-dioxolane (DOL) and DME (DOL : DME = 1 : 1, by volume) with 2 wt% $LiNO_3$ as an additive to promote stable SEI layer formation. Celgard 2300 (19 μm, PP/PE/PP) was utilized as the separator.

Battery performance was evaluated using a Neware battery tester at 25 °C in galvanostatic mode at varying current densities. Half cells were constructed using NF-NiO or NF as working electrodes and a Li piece (450 μm in thickness) as the counter electrode. The Li plating/stripping CE was assessed by discharging half cells at 1 mA cm^{-2} for 1 h, followed by charging to 1.5 V. NF-NiO was pre-lithiated in a half-cell to achieve a Li loading of 4 mAh cm^{-2}, after which the half cells were disassembled in a glovebox to obtain NF-NiO@Li. Symmetric cells were assembled using NF-NiO@Li for both electrodes and subjected to charge–discharge cycles at constant current densities of 1 mA cm^{-2} and 0.5 mA cm^{-2} to 1 mAh cm^{-2} to examine interface stability and electrode polarization. For full-cell testing, $LiFePO_4$ cathodes (areal capacity ~2.65 mAh cm^{-2}) were assembled with NF-NiO. Following SEI layer stabilization through three cycles at 0.1C, cyclic testing was performed between 2.6–3.8 V at current densities ranging from 0.1–1C. Electrochemical impedance spectroscopy (EIS) measurements were conducted using a CHI660C electrochemical workstation across frequencies from 0.01 Hz to 0.1 MHz.

2.4. Construction of *in situ* cell

To examine the deposition mechanism and morphology of metallic lithium on NF-NiO, three distinct half-cells (Li‖Cu, Li‖NF, and Li‖NF-NiO450) were fabricated using the *in situ* electrochemical cell configuration shown in Fig. S1. Each cell incorporated a pre-cut 1 cm × 1 cm lithium metal anode coupled with the corresponding cathodes (Cu foil, NF, or NF-NiO450). The morphological evolution of lithium deposition during cation migration and metal electroplating was observed through *in situ* polarized light microscopy at 5000× magnification. Systematic time-resolved imaging was conducted, with representative micrographs captured during significant morphological changes in lithium nucleation and growth processes.

3. Results and discussion

3.1. Morphology and characterization of the NF-NiO

The preparation of nickel foam modified with nickel oxide (NF-NiO) involved acid-washing and air annealing processes under various temperature gradients, as illustrated in Fig. S2. The acid etching of NF in HNO_3 produced a green solution due to the presence of Ni^{2+} ions (Fig. S3a).

When heated above 400 °C, metallic nickel transforms into a mixture of NiO and Ni_2O_3. At approximately 400 °C, NiO reacts with atmospheric oxygen to form Ni_2O_3 (reaction (1), which subsequently reduces back to NiO at around 600 °C (reaction (2).

$$4NiO + O_2 \rightarrow 2Ni_2O_3 \quad (1)$$

$$2Ni_2O_3 \rightarrow 4NiO + O_2 \quad (2)$$

Based on these reactions, three temperatures – 400 °C, 450 °C, and 500 °C – were selected for the heat treatment of nickel foam during air annealing. This selection enabled the investigation of the nickel oxide composition formed at each temperature and the influence of NiO and Ni_2O_3 on the modified current collector's performance. Fig. S3b–e shows optical photographs of the NF-NiO electrodes after annealing at various temperatures. The untreated NF exhibits a silvery-white, porous metallic appearance. Upon annealing at 400 °C, the NF foam substrate develops a yellow coloration. With increasing annealing temperature, the NF-NiO surface progressively darkens, becoming entirely black at 500 °C.

The electrode's color change may indicate a phase transition, necessitating XRD characterization to determine the phase and composition of NF-NiO. As shown in Fig. 2l, the distinction between NiO and Ni_2O_3 content in NF-NiO samples annealed at different temperatures remains indistinct in XRD analysis. Nevertheless, diffraction peaks at 44.62°, 51.97°, and 76.48° in the NF sample align with the standard nickel card (PDF#87-0712), corresponding to the (111), (200), and (220) crystal planes.[30] The NF-NiO sample exhibits both NF and Ni oxidation peaks at 37.06, 43.1, 62.6, 75.090, and 79.185. These diffraction peaks correspond to cubic nickel oxide crystal peaks with diffraction planes (111), (200), (220), (311), and (222).

SEM images were obtained to examine the morphological characteristics of the Ni foam sample. As illustrated in Fig. 2a–e and Fig. S4, the base NF exhibits a three-dimensional structure with micrometer-sized pores. The untreated NF skeleton presents a smooth surface, which does not facilitate lithium metal nucleation and deposition. In contrast, island-like protrusions and granular textures occur in NF-NiO at all three temperatures. Compared to NF-NiO400, NF-NiO450 exhibits denser and more refined island-shaped protrusions. However, NF-NiO500 displays branching cracks without complete fracture, consistent with high-temperature-induced degradation of mechanical stability described subsequently. Furthermore, the surface of NF-NiO450 develops nanometer-sized micropores. These surface irregularities enhance lithium metal nucleation on the electrode surface, promoting more uniform metallic lithium deposition morphology.

X-ray photoelectron spectroscopy (XPS) analysis was conducted to determine the chemical composition of the NF-NiO material and investigate how different oxidation states of Ni influence battery cycling performance. The results are presented in Fig. 2g–k. All three samples exhibited $Ni2p_{1/2}$, $Ni2p_{3/2}$, and two satellite peaks. The $Ni2p_{3/2}$ peak revealed both Ni^{2+} and Ni^{3+} peaks, indicating NiO and Ni_2O_3 formation. Specifically, $Ni2p_{3/2}$ (853.9 eV) corresponds to Ni^{2+} binding energy, while $Ni2p_{3/2}$ (857.3 eV) represents Ni^{3+} binding energy.[36] The proportion of Ni^{3+} and Ni^{2+} in each sample was calculated from the binding energy peak areas in the Ni 2p spectrum. Ni^{3+} comprises 47.7%, 67.8%, and 58.6% of the total Ni elements in NF-NiO400,

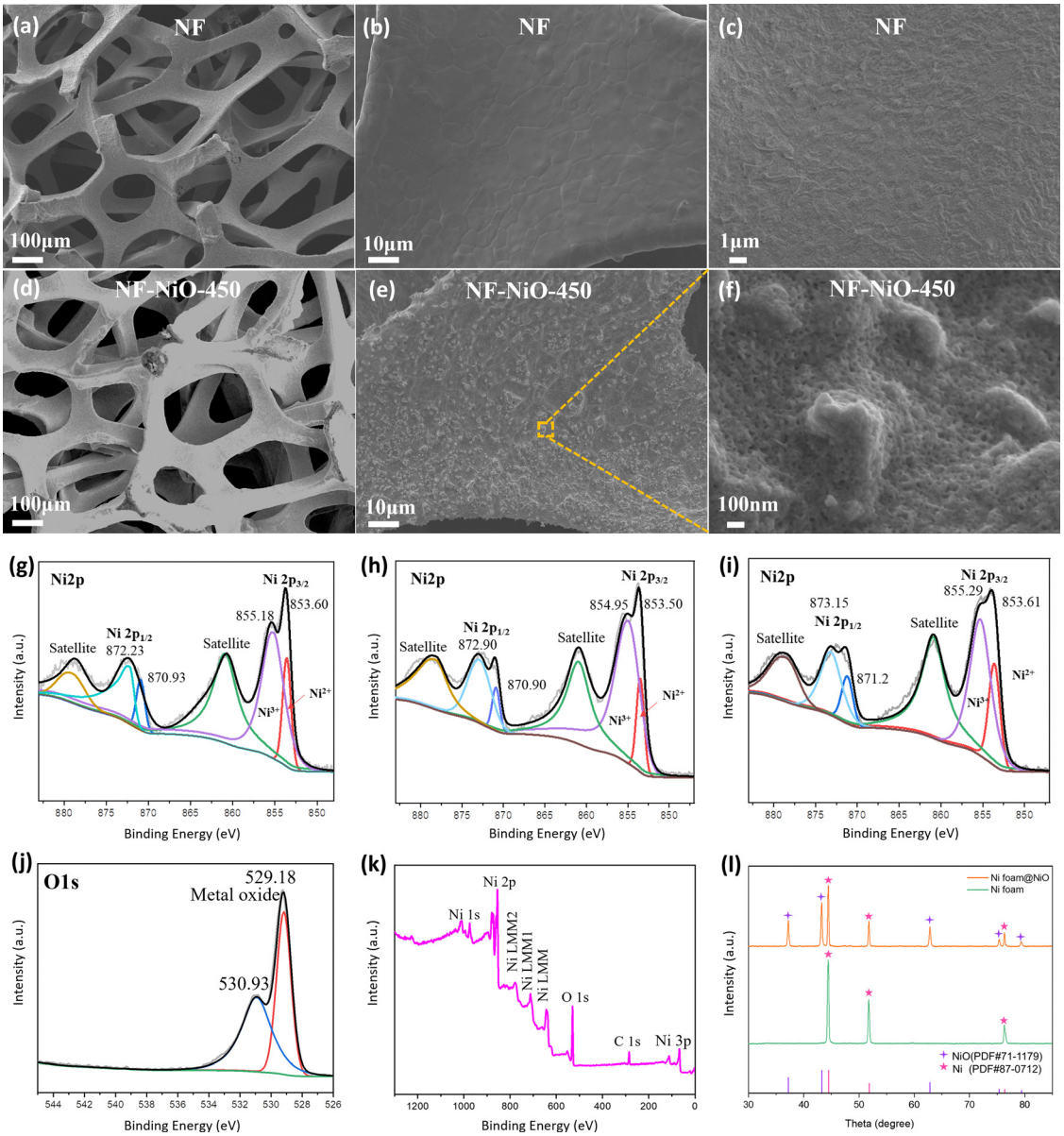

Fig. 2 Morphological characterizations of different samples: (a)–(c) Nickel foam; (d)–(f) NF-NiO450. X-ray photoelectron spectra of (g) NF-NiO400, (h) NF-NiO450 and (i) NF-NiO500 composite electrodes. (j) O 1s energy spectrum and (k) XPS full spectrum of NF-NiO450. (l) XRD spectra of NF and NF-NiO.

NF-NiO450, and NF-NiO500, respectively (Fig. S5). NF-NiO450 material exhibited the highest Ni^{3+}/Ni^{2+} ratio, while both NF-NiO400 and NF-NiO500 exhibited decreased ratios, suggesting that extreme temperatures impede Ni^{3+} (Ni_2O_3) production. Fig. 2i displays the O 1s absorption peak spectrum, showing two chemical states at 529.18 eV and 531.93 eV for the NF-NiO450 nickel oxide thin film. The O 1s binding energies of 529.18 eV and 531.93 eV correspond to NiO and Ni_2O_3, respectively. Fig. 2j presents the full spectrum absorption peak, revealing Ni 1s, Ni 2p, O 1s, C 1s, and Ni 3p absorption peaks, confirming previous analytical findings.

3.2. Electrochemical performances

Half-cells were assembled using NF-NiO400, NF-NiO450, NF-NiO500, NF-NiO600, and NF with a 450 μm thick lithium slice. The electrochemical performance of NF samples treated at different temperatures was evaluated by cycling under conditions of 1 mA cm^{-2}, 1 mAh cm^{-2} and 2 mA cm^{-2}, 1 mAh cm^{-2}. Fig. S6 demonstrates that the NF-NiO600 sample exhibited unstable cycling in the CE of the electrochemical test, displaying capacitor-like charge–discharge characteristics. This suggests that an excessive annealing temperature compromises the mechanical stability of foam nickel, preventing the maintenance of a structure conducive to metallic lithium nucleation. NF, characterized by poor lithiophilicity, demonstrated limited cycling performance, maintaining steady cycling for approximately 75 cycles with a CE of 96.6% under test conditions of 1 mA cm^{-2}, 1 mAh cm^{-2} (Fig. 3a). The NF-NiO electrodes treated at various temperatures exhibited improved CE compared to NF, highlighting the role of lithiophilic nickel oxide[31] in enhancing cycle stability and promoting uniform lithium

deposition. The NF-NiO500 electrode maintained a stable cycling capacity for 220 cycles at 1 mA cm^{-2} and 1 mAh cm^{-2}. However, the CE exceeding 100% after approximately 150 cycles indicated an internal short-circuit caused by dendrite penetration of the separator. At an increased current density of 2 mA cm^{-2}, NF-NiO500 demonstrated reduced cycling stability, maintaining stable cycling for approximately 140 cycles with a CE of 97.3%. NF-NiO400 and NF-NiO450 demonstrated enhanced cycling stability and CE. The NF-NiO400 electrode exhibited excellent capacity retention, cycling steadily for 250 cycles at 96.8% CE, while NF-NiO450 cycled for 330 cycles at 97.67% CE under 1 mA cm^{-2} and 1 mAh cm^{-2} conditions. Under a 2 mA cm^{-2} current density, NF-NiO400's CE declined after 180 cycles, while NF-NiO450 maintained 97.3% for 220 stable cycles. NF-NiO450 demonstrated superior CE and cycling stability compared to other NF-NiO and NF substrates.

Fig. 3c illustrates the capacity–voltage curves under 1 mA cm^{-2} conditions. The nucleation overpotential of NF reached a maximum of 0.53 V, while NF-NiO450 exhibited the lowest at 0.17 V, representing a significant reduction. The reduced nucleation overpotential indicates decreased resistance to lithium nucleation on the NF-NiO450 surface, confirming its enhanced lithiophilicity. The EIS impedance spectrum results shown in Fig. 3d reveal that the NF-NiO450 sample exhibits the smallest impedance circle radius in the high-frequency region, indicating the lowest nucleation impedance among other specimens.[37]

The electrochemical performance of the NF-NiO450@Li symmetric cell was evaluated at current densities of 0.5 mA cm^{-2} and 1 mA cm^{-2} to assess the interfacial stability and polarization characteristics of the NF-NiO450 electrode. Fig. 3e–h present the test results of the symmetric cell at a current density of 0.5 mA cm^{-2} and a deposition capacity of 1 mAh cm^{-2}. The Li electrode and NF-NiO450 demonstrated stable polarization voltages of 9 mV and 13 mV, respectively. After 500 h of cycling, the Li electrode exhibited a gradual increase in polarization voltage, while the NF-NiO450 electrode maintained stability until 900 h. At this point, the Li electrode's polarization voltage increased to 50 mV, indicating an irreversible impedance increase. The cycling results at 1 mA cm^{-2} are shown in Fig. 3i–l. The NF@Li electrode exhibited a decrease from a higher polarization voltage, suggesting a soft short-circuit occurrence. The polarization voltage subsequently stabilized at 54 mV before complete failure due to a short circuit after approximately 300 h. The Li electrode demonstrated a lower polarization voltage compared to NF@Li, stabilizing at 18 mV after a brief initial increase. NF-NiO450@Li displayed superior performance with the lowest and most stable polarization voltage of 10 mV for over 700 h. However, the Li anode showed an increased polarization voltage after 600 h of cycling, indicating enhanced interfacial impedance and reduced interfacial stability.[38] These results demonstrate that the NF-NiO450 electrode facilitates more uniform lithium metal deposition through NiO's lithiophilicity, contributing to improved interfacial stability of the lithium metal electrode.

The characterization results indicate that annealing at 450 °C produces a higher ratio of Ni_2O_3. Ni_2O_3 exhibits superior conductivity compared to NiO (Fig. S7), and Ni_{III} demonstrates higher oxidative properties than Ni_{II}.[39] Limited conductivity results in significant internal resistance, substantial polarization, and inferior lithium deposition kinetics during extended cycling. Thus, achieving a higher proportion of Ni_2O_3 facilitates surface charge transfer, while its enhanced oxidizing properties improve lithiophilicity, which was also proved by density functional theory

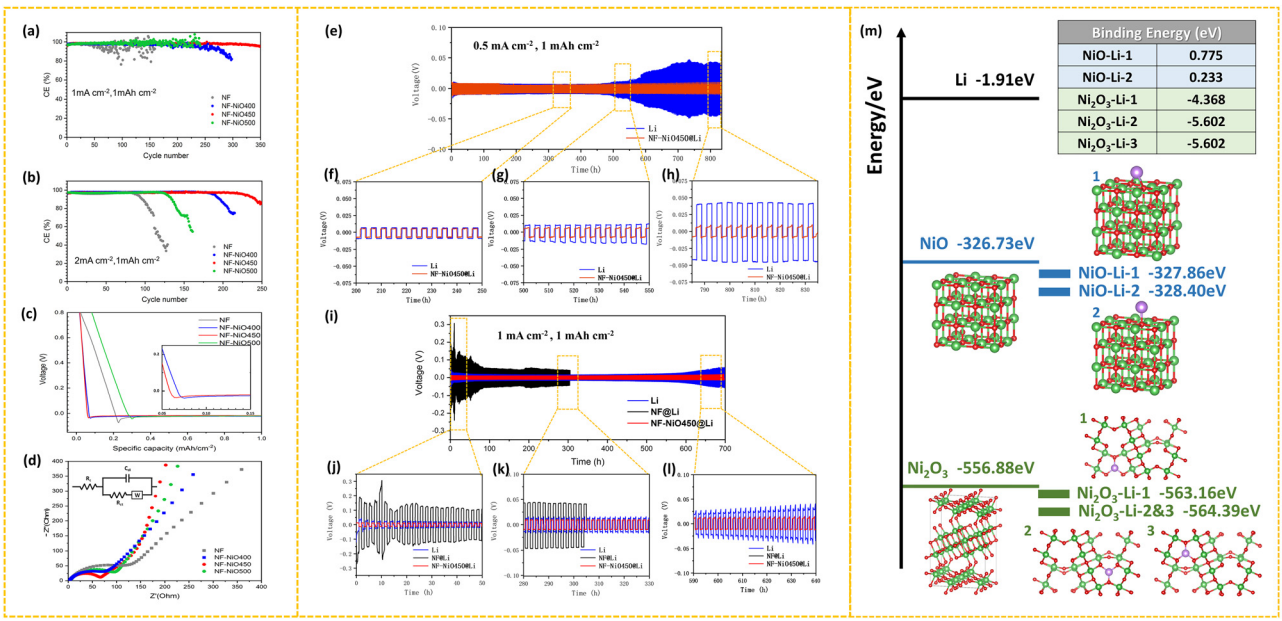

Fig. 3 Electrochemical performance results of NF-NiO and NF half-cell tests and symmetric cells: Coulomb efficiency test results at (a) 1 mA cm^{-2}, 1 mAh cm^{-2} and (b) 2 mA cm^{-2}, 1 mAh cm^{-2}. (c) Capacity–voltage curve of each electrode at 1 mA cm^{-2} current density. (d) EIS curve of the AC impedance spectrum of the first cycle of the half-cell. Voltage–time curves for symmetric cells under the current densities of (e)–(h) 0.5 mA cm^{-2} and (i)–(l) 1 mA cm^{-2}. (m) Density functional theory calculation of the binding energies of various possible structures of Ni_2O_3 and NiO with Li.

(DFT) calculation (Fig. 3m). These findings align with the electrochemical test results, where the NF-NiO450 electrode, containing a higher proportion of Ni_2O_3, exhibits superior electrochemical performance.

3.3. Analysis of lithium deposition behavior on NF-NiO current collector

To examine the deposition behavior of lithium metal on NF-NiO, lithium metal was deposited on NF and NF-NiO450 electrodes at a current density of 0.5 mA cm^{-2}, producing high-capacity lithium metal. The discharge/charge capacity–voltage curve of the NF-NiO450 electrode is presented in Fig. S8. The areal capacity of the deposited Li metal achieved 12 mAh cm^{-2}, indicating the substantial lithium loading capability of this current collector.

The morphological evolution of lithium deposition observed through *in situ* polarized light microscopy (Fig. 4) and scanning electron microscopy (Fig. 5) reveals distinct nucleation and growth mechanisms. As illustrated in Fig. 4a, the Li‖Cu configuration demonstrated the most rapid lithium growth kinetics, with prominent lithium dendrites emerging within 39 minutes of discharge initiation, characterized by loosely packed metallic lithium with significant internal porosity. The Li‖NF cell exhibited controlled deposition kinetics (Fig. 4b), where the nickel foam's three-dimensional structure directed preferential lithium nucleation within its pores, effectively managing volume expansion. Surface protrusions became visible only after 58 minutes of operation. Fig. 4c demonstrates a distinctly different deposition pattern on NF-NiO450, with initial speckled nuclei appearing at minute 80, followed by systematic lateral propagation of lithium clusters around these nucleation sites. Supplementary SEM characterization (Fig. 5) provided detailed verification of these morphological evolution processes, confirming the substrate-dependent lithium plating/stripping dynamics. Following 2 mAh cm^{-2} of Li deposition on the electrode, irregular agglomerated lithium deposition formed on the NF electrode surface, with lithium metal accumulating on the electrode surface. The NF-NiO450 electrode facilitated the formation of smaller crystal nuclei, reducing the lithium aggregation phenomenon. As deposition capacity increased, a loose deposition morphology developed on the NF surface, characterized by worm-like lithium metal formation accompanied by small dendrites. At 8 mAh of lithium deposition, the NF electrode surface exhibited significant irregular deposition, with crack formation in certain areas and lithium proliferation at these protrusions, generating substantial "dead lithium". Conversely, the lithium affinity of NiO enhanced electron transfer,[40] resulting in a uniform lithium deposition layer on the NF-NiO450 surface. Even after 8 mAh of metal deposition, the morphology remained smooth and compact without apparent dendrites or mossy formations. This suggests that the lithium-affinitive nickel oxide surface of the NF-NiO450 electrode provides numerous nucleation sites for lithium deposition. Additionally, its three-dimensional matrix structure effectively mitigates lithium metal volume expansion.

3.4. Full-cell performance of NF-NiO

To evaluate the practical application potential of the NF-NiO current collector in lithium metal anodes, a full cell was assembled using the current collector with a commercial cathode. The commercially available lithium iron phosphate ($LiFePO_4$) cathode material, with a areal capacity of 2.65 mAh cm^{-2}, was selected. $LiFePO_4$ was chosen for its stable structure, which provides exceptional cycle stability and serves as a standard for evaluating lithium metal anode cycle stability.[41] The full-cell testing was conducted in an ether electrolyte system with the battery structure illustrated in Fig. 6a. Prior to testing, electrochemical pre-lithiation deposited 4 mAh of metallic lithium on the electrode surface, maintaining an N/P ratio of 1.51. Fig. 6b demonstrates the rate test results of the NF-NiO450@Li anode full cell. During rate testing from 0.1C to 1C, the NF-NiO450@Li exhibited areal capacities of approximately

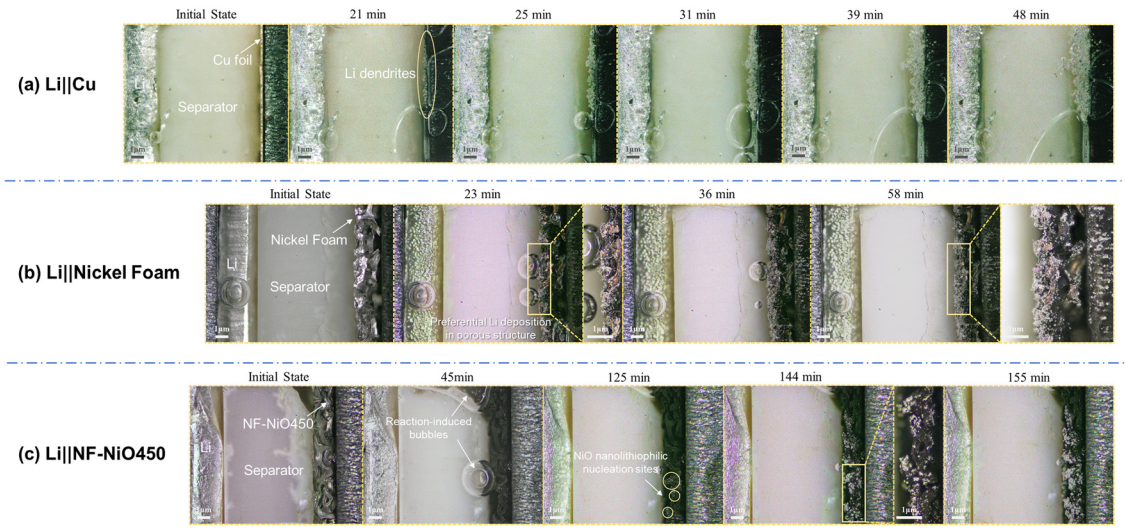

Fig. 4 The deposition morphology of metallic lithium on the current collector in *in situ* cells observed under an *in situ* polarized light microscope: (a) Li‖Cu, (b) Li‖NF, and (c) Li‖NF-NiO450.

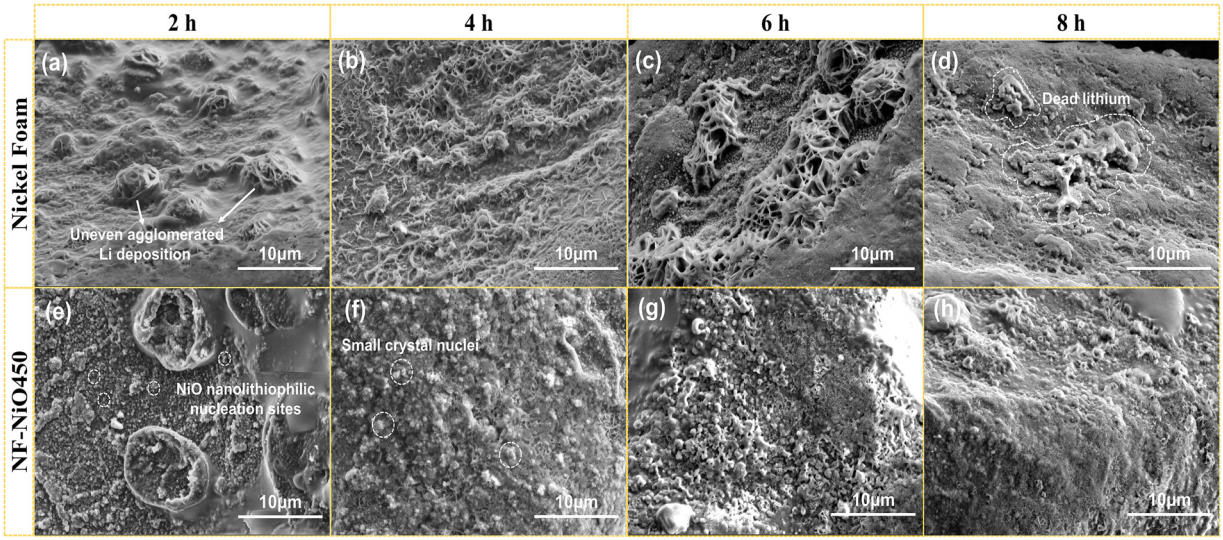

Fig. 5 Top-view SEM images of various anodes with lithium deposition of (a) and (e) 2 mAh cm^{-2}; (b) and (f) 4 mAh cm^{-2}; (c) and (g) 6 mAh cm^{-2} and (d) and (h) 8 mAh cm^{-2}.

3.25 mAh cm^{-2}, 3.0 mAh cm^{-2}, 2.75 mAh cm^{-2}, and 2.65 mAh cm^{-2}, respectively. Upon returning to 0.1C after high-rate cycling at 1C, the capacity recovered to approximately 3.2 mAh cm^{-2}. As illustrated in Fig. 6, the NF-NiO450@Li electrode demonstrated stable cycling for over 160 cycles at a low N/P ratio (~1.51) and 1C rate during long-cycle testing, maintaining a capacity retention rate of 92.42% and exhibiting excellent cycle reversibility. The comparison of capacity retention rates of some 3D collectors used in LMBs, shown in Fig. 6f, also illustrates this point.[42–50] The capacity–voltage curve (Fig. 6e) indicates a minimal increase in overpotential with increasing cycles, suggesting robust interfacial stability.

4. Conclusion

This study successfully developed a microporous structure on the nickel foam surface with nickel oxide particles through air annealing, substantially enhancing the electrochemical performance of the nickel foam substrate. The modification method demonstrates significant potential for nickel oxide-modified current collectors in facilitating uniform lithium metal deposition. The high specific surface area of nickel foam enhances reactant adsorption and diffusion, thereby improving battery performance. Furthermore, this research examined how the valence state of nickel oxide-modified nickel foam influences

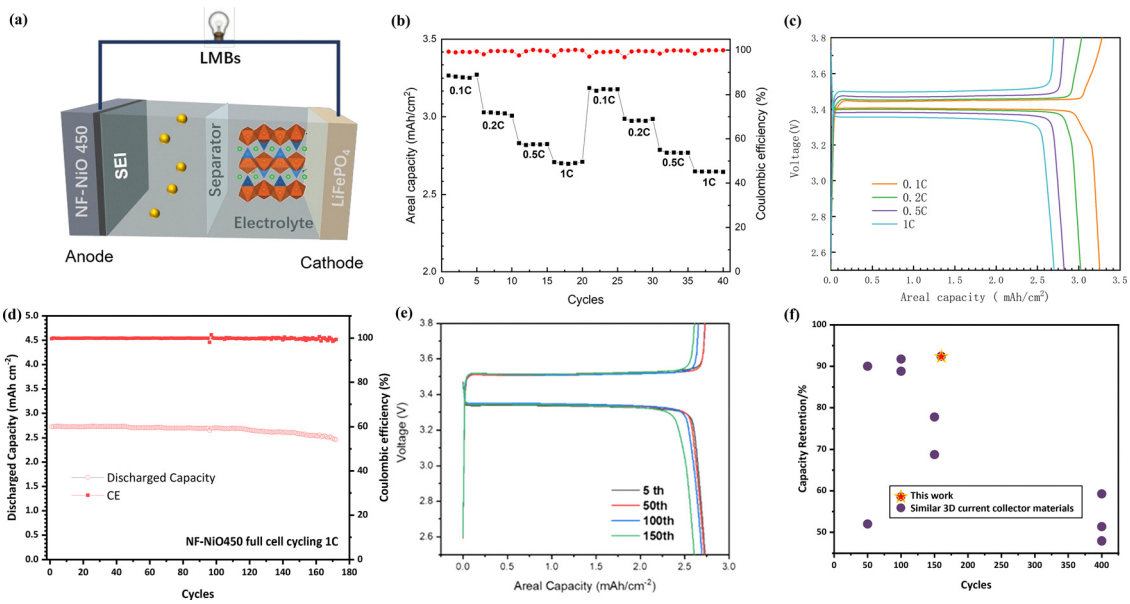

Fig. 6 (a) Schematic configuration of NF-NiO450@Li‖$LiFePO_4$. Rate performance (b) and (c) and long-cycle performance (d)–(e) of the NF-NiO450 anode-assembled full cell with the $LiFePO_4$ cathode. (f) Comparison of capacity retention rates of partial 3D current collectors used in LMBs.

electrode electrochemical performance. Ni_2O_3 exhibits superior conductivity and stronger oxidizing properties compared to NiO. NF-NiO450, containing a higher proportion of Ni_2O_3, demonstrates superior electrochemical performance, achieving the lowest nucleation overpotential of 0.17 V and maintaining a high CE of 97.67% over 330 cycles. In symmetric cell testing, the NF-NiO450 electrode exhibits a minimal polarization voltage of 10 mV at 1 mAh cm^{-2}, indicating that higher-valence nickel oxide more effectively induces uniform lithium metal nucleation and deposition. A full cell incorporating $LiFePO_4$ as the positive electrode and NF-NiO450@Li as the negative electrode, with an N/P ratio of 1.51, demonstrates stable cycling exceeding 180 cycles at 1C, maintaining a capacity retention rate of 90.2%. The temperature-controlled nickel oxide-modified nickel foam current collector exhibits exceptional full-cell cycle stability and high capacity, indicating substantial practical application potential. This research provides insights for further modifications of three-dimensional skeleton materials, offers enhanced lithium-friendly sites for high-energy lithium metal battery anodes, and advances the development of practical and safe LMBs.

Author contributions

Yao Li and Di Zhang conceived the ideas and designed the experiments. Hao He, Zhao Yu, Yongsheng Hu, Yanjie Liu, Yanyu Li and Shenmin Zhu were involved in the methods and characterizations of materials. Hao He and Zhao Yu analysed the data and wrote the manuscript. Yue Miao participated in discussions and modifications. All the authors discussed the results and commented on the manuscript.

Conflicts of interest

There are no conflicts to declare.

Data availability

Data are provided within the manuscript or supplementary information (SI). Supplementary information is available. See DOI: **https://doi.org/10.1039/d5ma00669d**.

Acknowledgements

This research was supported by The National Key Research Development Program of China (2021YFB3800300), Shanghai Pujiang Programme (23PJD045) and The National Natural Science Foundation of China no. 22479097.

References

1 D. Wang, W. Zhang, W. Zheng, X. Cui, T. Rojo and Q. Zhang, *Adv. Sci.*, 2016, **4**, 1600168.
2 L. Liu, Y. X. Yin, J. Y. Li, S. H. Wang, Y. G. Guo and L. J. Wan, *Adv. Mater.*, 2018, **30**, 1706216.
3 Q. Li, S. Zhu and Y. Lu, *Adv. Funct. Mater.*, 2017, **27**, 1606422.
4 D. Lin, Y. Liu and Y. Cui, *Nat. Nanotechnol.*, 2017, **12**, 194–206.
5 X.-B. Cheng, R. Zhang, C.-Z. Zhao and Q. Zhang, *Chem. Rev.*, 2017, **117**, 10403–10473.
6 N. Li, X. Han, X. Cui, C. Xu, C. Mao, X. Dai and W. Xue, *Adv. Funct. Mater.*, 2024, 35.
7 G. Zhou, F. Li and H.-M. Cheng, *Energy Environ. Sci.*, 2014, **7**, 1307–1338.
8 H. Cai, X. Cui, Y. Shi, Y. Zhang, X. Chen, L. Fan, J. Zhou, C. Tian and W. Xue, *ACS Nano*, 2024, **18**, 32723–32731.
9 H. J. S. Sand, *Proc. Phys. Soc., London*, 1899, **17**, 496.
10 X. Zhang, A. Wang, X. Liu and J. Luo, *Acc. Chem. Res.*, 2019, **52**, 3223–3232.
11 J. Liu, H. Yuan, H. Liu, C. Z. Zhao, Y. Lu, X. B. Cheng, J. Q. Huang and Q. Zhang, *Adv. Energy Mater.*, 2021, **12**, 2100748.
12 Y. S. Cohen, Y. Cohen and D. Aurbach, *J. Phys. Chem. B*, 2000, **104**, 12282–12291.
13 R. Chen, M. Yu, R. P. Sahu, I. K. Puri and I. Zhitomirsky, *Adv. Energy Mater.*, 2020, **10**, 1903848.
14 F. Liu, R. Xu, Y. Wu, D. T. Boyle, A. Yang, J. Xu, Y. Zhu, Y. Ye, Z. Yu, Z. Zhang, X. Xiao, W. Huang, H. Wang, H. Chen and Y. Cui, *Nature*, 2021, **600**, 659–663.
15 C.-P. Yang, Y.-X. Yin, S.-F. Zhang, N.-W. Li and Y.-G. Guo, *Nat. Commun.*, 2015, **6**, 8058.
16 C. Brissot, M. Rosso, J.-N. Chazalviel and S. Lascaud, *J. Power Sources*, 1999, 81–82.
17 F. Ding, W. Xu, G. L. Graff, J. Zhang, M. L. Sushko, X. Chen, Y. Shao, M. H. Engelhard, Z. Nie, J. Xiao, X. Liu, P. V. Sushko, J. Liu and J.-G. Zhang, *J. Am. Chem. Soc.*, 2013, **135**, 4450–4456.
18 J. N. Chazalviel, *Phys. Rev. A*, 1990, **42**, 7355–7367.
19 C. Guo, Y. Guo, R. Tao, X. Liao, K. Du, H. Zou, W. Zhang, J. Liang, D. Wang, X.-G. Sun and S.-Y. Lu, *Nano Energy*, 2022, **96**, 10712.
20 J. Y. Kim, G. Liu, M. X. Tran, R. E. Anugrah Ardhi, H. Kim and J. K. Lee, *J. Mater. Chem. A*, 2019, **7**, 12882–12892.
21 C. D. Fincher, D. Ojeda, Y. Zhang, G. M. Pharr and M. Pharr, *Acta Mater.*, 2020, **186**, 215–222.
22 Y. Chen, X. Xu, L. Gao, G. Yu, O. O. Kapitanova, S. Xiong, V. S. Volkov, Z. Song and Y. Liu, *Small Methods*, 2022, **6**, 2200113.
23 P. Biswal, S. Stalin, A. Kludze, S. Choudhury and L. A. Archer, *Nano Lett.*, 2019, **19**, 8191–8200.
24 A. Pei, G. Zheng, F. Shi, Y. Li and Y. Cui, *Nano Lett.*, 2017, **17**, 1132–1139.
25 Y. He, X. Ren, Y. Xu, M. H. Engelhard, X. Li, J. Xiao, J. Liu, J.-G. Zhang, W. Xu and C. Wang, *Nat. Nanotechnol.*, 2019, **14**, 1042–1047.
26 J. Eaves-Rathert, K. Moyer, M. Zohair and C. L. Pint, *Joule*, 2020, **4**, 1324–1336.
27 K. Nishikawa, T. Mori, T. Nishida, Y. Fukunaka, M. Rosso and T. Homma, *J. Electrochem. Soc.*, 2010, **157**, A1212–A1217.
28 L. Zhang, T. Yang, C. Du, Q. Liu, Y. Tang, J. Zhao, B. Wang, T. Chen, Y. Sun, P. Jia, H. Li, L. Geng, J. Chen, H. Ye, Z. Wang, Y. Li, H. Sun, X. Li, Q. Dai, Y. Tang, Q. Peng,

T. Shen, S. Zhang, T. Zhu and J. Huang, *Nat. Nanotechnol.*, 2020, **15**, 94–98.
29 W. Hu, Y. Yao, X. Huang, S. Ju, Z. Chen, M. Li and Y. Wu, *ACS Appl. Energy Mater.*, 2022, **5**, 3773–3782.
30 X. Shen, S. Shi, B. Li, S. Li, H. Zhang, S. Chen, H. Deng, Q. Zhang, J. Zhu and X. Duan, *Adv. Funct. Mater.*, 2022, **32**, 2206388.
31 Z. Li, L. Huai, S. Li, M. Ma, K. Luo, Y. Zhao, D. Wang, X. Sun and Z. Peng, *Energy Storage Mater.*, 2021, **37**, 491–500.
32 X. Cui, S. Ding, Y. Niu, H. Wang, Y. Lu, Y. Hu and W. Xue, *Adv. Mater.*, 2025, **37**(12), 2415611.
33 Q. Huang, F. Wang, Z. Sun, B. Zhang, W. Li, F. Guo, Y. Liu, F. Ren and X. Duan, *Adv. Funct. Mater.*, 2024, **34**, 2407407.
34 H. Du, T. Wang, S. He, B. Li, K. Wang, Q. Chen, Z. Du, W. Ai and W. Huang, *Adv. Funct. Mater.*, 2023, **34**, 2311854.
35 X. Sun, Y. Xia, B. Wang, B. Li, L. Ma, J. Chen and B. Chi, *Chem. Eng. J.*, 2024, **479**, 147598.
36 S. R. Jiang, P. X. Yan, B. X. Feng, X. M. Cai and J. Wang, *Mater. Chem. Phys.*, 2002, **77**, 384–389.
37 W. Choi, H.-C. Shin, J. M. Kim, J.-Y. Choi and W.-S. Yoon, *J. Electrochem. Sci. Technol.*, 2020, **11**, 1–13.
38 Y. Xiao, Y. Wang, S.-H. Bo, J. C. Kim, L. J. Miara and G. Ceder, *Nat. Rev. Mater.*, 2019, **5**, 105–126.
39 K.-S. Ahn, Y.-C. Nah and Y.-E. Sung, *Appl. Surf. Sci.*, 2002, **199**, 10.
40 Z. Chen, W. Chen, H. Wang, C. Zhang, X. Qi, L. Qie, F. Wu, L. Wang and F. Yu, *Nano Energy*, 2022, **93**, 106836.
41 W.-J. Zhang, *J. Power Sources*, 2011, **196**, 2962–2970.
42 J. H. Um, H. Kim, Y.-H. Cho and W.-S. Yoon, *J. Electrochem. Sci. Technol.*, 2020, **11**, 92–98.
43 S. Huang, W. Zhang, H. Ming, G. Cao, L.-Z. Fan and H. Zhang, *Nano Lett.*, 2019, **19**, 1832–1837.
44 Y. Li, S. Li, J. Cui, J. Yan, H. H. Tan, J. Liu and Y. Wu, *Nanoscale Adv.*, 2022, **4**, 4639–4647.
45 S. Wang, C. Liu, M. Zhao, R. Song, Y. Lu, L. Gou, F. Gong, X. Fan and D. Li, *J. Power Sources*, 2024, **614**, 234960.
46 S. Zhang, Y. Ma, Y. Zhao, Y. Qian, L. Suo, X. Wang, J. Huang, W. Li and B. Zhang, *ACS Appl. Polym. Mater.*, 2023, **5**, 3289–3297.
47 J. Chen, G. Liu, X. Han, H. Wu, T. Hu, Y. Huang, S. Zhang, Y. Wang, Z. Shi, Y. Zhang, L. Shi, Y. Ma, H. N. Alshareef and J. Zhao, *ACS Nano*, 2024, **18**, 13662–13674.
48 W. Zhang, H. Jin, C. Xu, S. Zhao, Y. Du and J. Zhang, *J. Power Sources*, 2019, **440**, 227142.
49 X. You, Y. Feng, D. Ning, H. Yao, M. Wang, J. Wang, B. Chen, G.-H. Zhong, C. Yang and W. Wu, *Nano Lett.*, 2024, **24**, 11367–11375.
50 S. Z. Xiaoyong Fan, Y. Zhu, M. Jing, K. Wang, L. Zhang, J. Li, L. Xu, L. Gou and D. Li, *Acta Chim. Sin.*, 2022, **80**, 9.